HHS Public Access

Author manuscript

Ultrasound Med Biol. Author manuscript; available in PMC 2022 February 01.

Published in final edited form as:

Ultrasound Med Biol. 2021 February ; 47(2): 309–322. doi:10.1016/j.ultrasmedbio.2020.09.009.

Therapeutic Ultrasound Parameter Optimization for Drug Delivery Applied to a Murine Model of Hepatocellular Carcinoma

Arsenii V. Telichko[a,*], **Huaijun Wang**[a], **Sunitha Bachawal**[a], **Sukumar U. Kumar**[a], **Jagathesh C. Bose**[a], **Ramasamy Paulmurugan**[a], **Jeremy J. Dahl**[a]

[a]Department of Radiology, School of Medicine, Stanford University, Stanford, California, United States of America

Abstract

Ultrasound and microbubble (USMB) mediated drug delivery is a valuable tool for increasing the efficiency of the delivery of therapeutic agents to cancer while maintaining low systemic toxicity. Typically, selection of USMB drug delivery parameters used in current research settings are either based on previous studies described in the literature or are optimized using tissue-mimicking phantoms. However, phantoms rarely mimic *in vivo* tumor environments and the selection of parameters should be based on the application or experiment. In the following study, we optimized the therapeutic parameters of ultrasound drug delivery system to achieve the most efficient *in vivo* drug delivery using fluorescent semiconducting polymer nanoparticles (SPN) as a model nanocarrier. We show that voltage, pulse repetition frequency (PRF), and treatment time (i.e. number of ultrasound pulses per therapy area) delivered to the tumor can successfully be optimized *in vivo* to ensure effective delivery of the SPNs to models of hepatocellular carcinoma. The optimal *in vivo* parameters for USMB drug delivery in this study were 70 V (peak negative pressure of 3.4 MPa, mechanical index 1.22), 1 Hz PRF, and 100 sec therapy time. USMB mediated drug delivery using *in vivo* optimized ultrasound parameters showed up to 2.2 fold ($p < 0.01$) increase in drug delivery to solid tumors compared to phantom-optimized ultrasound parameters.

Keywords

HCC; sonoporation; drug delivery; microbubbles; ultrasound; therapy

Introduction

Hepatocellular carcinoma (HCC) is the most common liver cancer and the second leading cause of cancer-related deaths worldwide (Forner et al., 2018; Njei et al., 2015; Simard et al., 2012; Fattovich et al., 2004; Mittal and El-Serag, 2013). Surgical resection and chemotherapy are currently the most efficient treatment options for the early stages of the disease, while liver transplantation can be used for advanced stage disease (European Association for the Study of the Liver and European Organisation for Research and Treatment of Cancer, 2012; Mazzaferro et al., 2011; Llovet et al., 2005). Because the

*Corresponding Author: Arsenii Telichko, 3155 Porter Dr., Palo Alto, CA 94304, USA; telichko@stanford.edu.

disease is frequently detected at later stages, most treatment options are often limited or not available (Grolami et al., 2003; Bismuth et al., 1993; Michel et al., 1997; Mazzaferro et al., 1996). In addition, the lack of transplant organs and high risk of relapse (Grolami et al., 2003; Lau and Lai, 2007; Belghiti et al., 1991; Ercolani et al., 2003) introduce further challenges to currently existing treatment strategies. For patients with intermediate HCC stages, trans-arterial chemoembolization (TACE) is the most commonly offered therapy (Lo et al., 2002; Camm et al., 2002; Lencioni et al., 2013). However, TACE often results in further complications in liver functions in patients with existing cirrhotic liver disease (Vogel et al., 2018; Murata et al., 2013).

Using standard intravenous (IV) delivery of anticancer therapeutic agents, only a fraction (0.001%−0.01%) of the injected drug is delivered to the tumor site, while most of the drug is accumulated elsewhere in healthy tissues or cleared by excretion (Snipstad et al., 2017; Gerber et al., 2009; Kurdziel et al., 2011) (Babakhanian et al., 2018). Recent advancements in nanotechnology allow efficient drug loading onto Poly(lactic-co-glycolic acid) (PLGA) nanoparticles (NPs) with slow-releasing effect, but the size of such nanoparticles limits the entry in tumor vasculature and delivery exclusively depends on the tumor's enhanced permeability and retention effect (Wu and Chiu, 2013; Pu et al., 2014). It has been shown that ultrasound (US) can locally enhance drug delivery of large nanoparticles by the sonoporation effect, which increases the permeability of vessel walls or cell membranes (Bao et al., 1997). Microbubbles (MBs) are US contrast agents that expand and contract under low amplitude US pressure waves; this is referred to as stable cavitation (Datta et al., 2006). Above a particular pressure threshold, MBs can collapse to produce shock waves and rapid local temperature increases; a process known as inertial cavitation (Vignon et al., 2013). Inertial cavitation has been used to improve drug delivery to tumors and reduce systemic toxicity associated with current therapeutic strategies in tumors, including HCC (Wang et al., 2015; Chowdhury et al., 2018, 2016). Except in the brain, drug delivery using inertial cavitation is preferred over stable cavitation because of the increased drug penetration depth into the tumor (Wang et al., 2015; Lai et al., 2013; Zhou et al., 2016).

USMB-mediated enhancement of therapeutic microRNAs (miRNAs) delivery in tumors can also be used for regulating the expression of various cellular genes related to tumor development and drug resistance and can be used as a novel anti-cancer approach to sensitize tumor cells to low dose chemotherapy (Chowdhury et al., 2016; Hsu et al., 2012; Xu et al., 2011; Tsai et al., 2012; Jopling, 2012; Xu et al., 2012; Tomimaru et al., 2012; Zhu et al., 2012; Bao et al., 2013).

Thus far, the US therapy parameters reported for enhancing drug delivery to solid tumors via inertial cavitation have been mostly based on phantom studies (Wang et al., 2015; Chowdhury et al., 2016, 2018; Snipstad et al., 2017; Eggen et al., 2014) and are not necessarily optimal for *in vivo* conditions, because phantoms do not adequately represent the tumor microenvironment (Hyun et al., 2018). In previous studies by our group on HCC therapy with miRNA delivery (Wang et al., 2015; Chowdhury et al., 2016, 2018), a relatively high pulse repetition frequency (PRF) of 20 – 100 Hz were selected based on phantom studies in a tissue-mimicking phantom with a 3 mm diameter channel (Wang et al., 2015). Microbubbles were injected into the channel with a syringe without mimicking blood

flow or scaling microbubble concentration to *in vivo* values. Because the tumor vasculature is more complicated than tissue-mimicking phantoms, a high PRF may result in poorly perfused areas with low microbubble concentration, leading to inefficient therapy (Miller and Quddus, 2000; Snipstad et al., 2017).

In this study, we use semiconducting π-conjugated polymeric nanomaterials (SNPs) as a model nanocarrier and aim to investigate the optimization of US parameters for efficient drug delivery. While our long-term goal is to develop an US-guided therapy system capable of efficient, uniform drug-delivery across the entire tumor volume, the aim of this particular study was to determine the optimal *in vivo* US therapy parameters for drug delivery into tumors.

Materials and Methods

Cell Culture

Human HepG2 HCC cells (ATCC, Manassas, VA) were grown in a high glucose (4.5 g/L) Dulbecco's modified Eagles medium (Invitrogen, Carlsbad, CA) and were supplemented with 10% fetal bovine serum, L-glutamine (2 mM), penicillin (100 U/mL), and streptomycin (100 μg/mL). Cells were incubated at 37 °C in a humidified atmosphere of 5% CO_2, and 95% air, and were grown to 70–80% confluency prior to trypsinization and preparation for tumor implantations.

Human Hepatocellular Carcinoma Xenografts in Mice

This study was approved by the Stanford University's Institutional Administrative Panel on Laboratory Animal Care. 5×10^6 of human HepG2 HCC cells were suspended in 50 μL of Matrigel (BD Biosciences, San Jose, CA), and then injected subcutaneously on both flanks of the hind limbs of female nude mice ($n = 30$, Charles River, 6–8 weeks old, weighing 20–25 g). Tumors were allowed to grow for 2–3 weeks after tumor cell injection until the tumors reached approximately 5 mm in diameter. Therapeutic US parameter optimization was carried out on one of the tumors, while the other tumor served as an intra-animal control.

Semiconducting π-Conjugated Polymeric Nanomaterials

Near-infrared (NIR) light absorbing SPNs were used as a model nanocarrier to confirm an entry of nanoparticles into the subcutaneous HCC via immunofluorescence (IF) confocal microscopy. SPNs are fluorescent nanomaterials made from organic and non-toxic materials and can be synthesized within a defined range of sizes (Pu et al., 2014; Ianni et al., 2019), with physicochemical properties similar to PLGA-NPs; however, they are unable to deliver therapeutics such as miRNA. Fluorescence SPNs were synthesized as reported previously (Pu et al., 2014) with minor modifications. In brief, 1,2-Distearoyl-sn-glycero-3-phosphoethanolamine (polyethylene glycol)-2000] (ammonium salt) (DSPE-PEG, 15 mg) was dissolved into a CH_2Cl_2 solution of Poly[2,7-(9,9-dioctylfluorene)-alt-4,7-bis(thiophen-2-yl) benzo-2,1,3-thiadiazole] PFO-DBT (0.25 mg/mL, 1 mL). The mixture was then rapidly poured into deionized distilled water (10 mL) under continuous sonication with an ultrasonic sonifier (Branson Ultrasonics, Danbury, CT) at a power output of 6 W

for 10 min on ice. The CH_2Cl_2 was then evaporated at 45 °C under a nitrogen atmosphere. Finally, the aqueous solution was filtered through a polyvinylidene fluoride (PVDF, 0.22 μm, MilliporeSigma, Burlington, MA) syringe driven filter. The resulting nanoparticle solution was stored in the dark at 8 °C. The average size of synthesized PEG-SPN was measured to be 110±15 nm with a Zetasizer Nano ZS90 sizing device (Malvern Pan-alytical Ltd., Malvern, U.K.). The absorption and emission maxima were at 523 nm and 630 nm respectively, as obtained by a spectrophotometer (Agilent 8453 spectrophotometer, Agilent Technologies, Santa Clara, CA) and a wavelength-calibrated fluorometer (FluoroMax-3, Horiba Jobin Yvon, Kyoto, Japan).

Ultrasound System

A Verasonics Vantage 256 scanner (Verasonics Inc., Redmond, WA) was used to perform image guidance and apply therapeutic pulses for drug delivery. Unlike our previous miRNA delivery experiments (Chowdhury et al., 2016, 2018) that utilized a dual-transducer design, a single high-frequency L11–5 transducer (ATL, Philips Healthcare, Netherlands) was used in this study for both therapy and imaging, as shown in Figure 1.

Transducer Calibration

The L11–5 transducer was characterized in a water tank filled with degassed deionized water. An Acoustic Intensity Measurement System (AIMS III, Onda, Sunnyvale, CA) was used to precisely raster-scan a hydrophone (HNR-0500, Onda, Sunnyvale, CA) in water to record the ultrasound pulse emitted from the L11–5 transducer, which was digitized and saved on an oscilloscope (Agilent DSO6012a, Santa Clara, CA). Further calculations, such as pressure field, intensities, peak negative pressure (PNP), and mechanical index (MI), were performed offline using MatLab (R2015b, MathWorks Inc., Natick, MA).

For pressure field characterization, a focused excitation at 8 mm depth with 50 V was used with the therapeutic US parameters shown in Table 1. The hydrophone was placed at the focal point of the beam and the full-width at half-maximum (FWHM, –6dB pressure area) in the axial, lateral, and elevation directions were measured. With the hydrophone in the center of the focal region, the applied voltage was then varied from 10 V to 50 V to measure PNP. To avoid damage to the hydrophone, pressure values were extrapolated linearly above 50 V up to a maximum of 90 V.

Ultrasound Therapy

Therapeutic US parameters not subjected to optimization are shown in Table 1. An F/2 transmit was used and 25 US cycles were applied for microbubble destruction. Voltage, PRF, and treatment time (number of pulses per focal region) were optimized as described in the Section Ultrasound Parameter Optimization. For the *in vivo* drug delivery experiments, 11 therapeutic pulses were laterally translated by the FWHM of the US beam, measured previously.

Ultrasound Image Guidance

For image guidance, a contrast-enhanced ultrasound sequence (CEUS) with pulse inversion (Averkiou et al., 2003; Couture et al., 2009; Couture et al., 2012) was utilized; the US

imaging parameters are summarized in Table 1. A plane-wave synthetic aperture imaging sequence was utilized, with 25 planes steered between ±10° per frame and spaced 0.8° apart. The beamformed images were displayed on the Verasonics scanner with a dynamic range of 60 dB at a frame rate of approximately 20 frames per second (FPS). Therapeutic focal regions were overlain on top of the CEUS image, as shown in Figure 1.

Microbubbles

Commercially available microbubbles such as MicroMarker (Bracco, Geneva, Switzerland; VisualSonics, Toronto, ON, Canada), BR38 (Bracco, Geneva, Switzerland), Definity (Lantheus Medical Imaging, North Billerica, MA, USA), and SonoVue (Bracco, Milan, Italy) microbubbles were used in this study. Microbubbles were activated using the conventional protocol provided by each vendor. The mean concentration and size of the microbubbles were measured on a particle counter (Z2 Coulter Counter, Beckmann Life Sciences Division, Indianapolis, IN). A total of 4 mice were used to select the microbubble for imaging with the previously described system.

In vivo *Protocol*

All mice were anesthetized with 2% isoflurane in the air (administered at 2 L/min) and placed on a heated platform in the prone position. A catheter was inserted into the tail vein for microbubble injection. A dedicated preclinical imaging system (Vevo 2100; VisualSonics, Toronto, Canada) with a high-frequency transducer for small animal imaging (MS250; center frequency of 18 MHz) was used for evaluating necrosis and overall perfusion of tumors by using a bolus injection of 20 μL (4×10^6 MBs, suspended in saline) non-targeted MicroMarker microbubbles. Tumors that were well perfused with no necrosis were used for the study.

After the tumor perfusion and absence of necrosis were visually confirmed on Vevo 2100 system, the L11–5 transducer was placed over the tumor with the therapeutic region targeting the tumor. For PRF and voltage optimization experiments, a continuous infusion of microbubbles was applied by using a power injection pump (GenieTouch, Kent Scientific, Torrington, CT). For experiments varying the treatment time and for direct comparison of the therapies with *in vivo*-optimized and phantom-optimized US parameters, a solution containing 75 μL of SPNs and 165 μL of microbubbles was mixed. Continuous injection with a flow rate of 50 μL/min of the microbubbles/mixture solution was established using the infusion pump. To ensure even flow of microbubbles in the circulation, all experiments were performed 90 sec after infusion was started. For the treatment time optimization and for direct comparison of the therapies with *in vivo*-optimized and phantom-optimized parameters, mice were euthanized 24 h after the experiments and the tumors were collected for further *ex vivo* IF analysis.

Ex vivo *Tissue Analysis*

Tumor tissues were fixed in 4% paraformaldehyde at 4 °C overnight and then cryopreserved in a 30% sucrose solution. Samples were then placed in optimal cutting temperature (OCT) compound and frozen immediately on dry ice. From each frozen sample, 10 μm sections were obtained by using a cryomicrotome. Sections were incubated in phosphate buffered

saline (PBS) for 10 min to remove the remaining OCT and permeabilized for 10 min in 0.5% Triton-X 100 in PBS. Sections were blocked in 3% bovine serum albumin solution (Sigma Aldrich, St. Louis, MO) containing 3% goat serum (Sigma Aldrich) and 3% donkey serum (Sigma Aldrich) for 30 min at room temperature prior to incubation with primary antibody of rabbit anti-mouse CD31 (Abcam, Cambridge, MA). The primary antibody of CD31 was visualized with AlexaFluor 546 goat anti-rabbit IgG secondary antibody (Invitrogen, Grand Island, NY).

Samples were imaged at 20x magnification with a TCS SP8 (Leica Microsystems, Buffalo Grove, IL) confocal microscope for the optimization of the treatment time and with an LSM710 metaconfocal microscope (Carl Zeiss GmbH, Jena, Germany) for comparison of the *in vivo*-optimized and phantom-optimized therapies. Initial image analysis was performed in ImageJ (National Institutes of Health, Bethesda, Maryland, U.S., and the Laboratory for Optical and Computational Instrumentation, University of Wisconsin).

To evaluate the amount of SPN delivered into the tumor and SPN penetration depth, quantitative image analysis was performed using Matlab. SPN and CD31 channels from IF images of the tumor samples were evaluated separately. For each channel, a pixel intensity threshold was set to be mean + 5x standard deviation of the pixel intensity in a background area where no vessel/SPN structures existed. This threshold was chosen to include fluorescent pixels from SPN or positive staining of CD31 and exclude pixels with autofluorescence (Wang et al., 2015; Eggen et al., 2013). Pixels with intensities below this threshold were considered interference from background fluorescence and were excluded. The distance from each SPN pixel signal to the nearest CD31 segment was computed, as well as the mean SPN signal intensity. The SPN signal intensity was normalized to the total area of CD31 (vessel area) and the total length of CD31 contour (vessel boundaries, whenever possible).

For hematoxylin and eosin (H&E) staining, tumor tissues were cryosectioned into 10 μm thick slices, and stained with H&E according to standard protocols for the presence of tissue damage by US treatment (Wang et al., 2015).

Ultrasound Parameter Optimization

PRF, voltage (i.e. pressure), and treatment time (i.e. number of therapeutic US pulses) were optimized *in vivo* to find the US parameters resulting in the most effective drug delivery. All remaining therapeutic US parameters were kept constant and are shown in Table 1. Schematic workflow of the ultrasound parameters optimization experiments is shown in Figure 2.

PRF and voltage

Microbubble perfusion time was measured directly by applying a single therapeutic US pulse and estimating the time required for microbubbles to perfuse back into the therapy region. CEUS imaging at 50 FPS was used to evaluate perfusion. 50 pre-therapy images were acquired followed by a single therapy pulse to induce inertial cavitation of microbubbles in the therapy region. 200 post-therapy image frames were then acquired. The pre- and post-therapy image frames were analyzed in MatLab and the time-intensity curve

inside the therapy region was calculated. To estimate the microbubble perfusion time, the intensity values were normalized to have a pre-burst mean and post-burst minimum values of 1 and 0, respectively, and the time-intensity curves were fit to

$$I(t) = 1 - exp\left(-t/t_p\right). \quad (1)$$

Here, t_p is the perfusion time in seconds and $I(t)$ is the measured intensity as a function of time t.

The perfusion time measurements were performed on 8 different mice on the left, middle, and right sides of both left and right tumors. All perfusion experiments were carried out with applied voltages of 70 V and 90 V, and the optimal PRF in Hz was calculated as

$$PRF_{opt} = 1/t_p. \quad (2)$$

Only high voltages were chosen for this experiment because high PNP values are required to induce inertial cavitation.

To confirm the consistency of the measured t_p, 100 ultrasound pulses with PRF_{opt} were delivered to the same focal region in the tumor, and time-intensity curves and perfusion times were computed after every 10 pulses.

Treatment Time

The total treatment time, or number of pulses per therapy region, was optimized to obtain the most efficient drug delivery *in vivo*. The number of pulses and total treatment time are related by the following equation:

$$\text{No of Pulses } = PRF_{opt} \times Treatment\ Time. \quad (3)$$

To obtain optimal treatment time, a series of experiments were performed using the previously optimized voltage and PRFopt. Ten mice were divided into 5 groups, with each group receiving therapy for 10, 30, 50, 75, and 100 seconds. IF was used to analyze the amount of SPN delivered to the HCC tumors and to select the optimal therapy time, as described in Section Ex vivo Tissue Analysis.

Comparison of in vivo-Optimized and Phantom-Optimized Therapy Parameters

Twelve mice were used to compare the drug delivery using the *in vivo*-optimized and phantom-optimized US parameters. Each mouse had one tumor that received the therapy while the other tumor was used as a negative control with no exposure to therapeutic US. Six mice received the treatment with US parameters that were optimized in phantoms, similar to those used in our previous studies (Chowdhury et al., 2018), and six mice received therapy with *in vivo*-optimized US parameters.

Results

Transducer Calibration

For the focused excitation from the L11–5 transducer at 7.8 MHz, the FWHM of the focal region was measured to be 0.65 × 8.5 × 2.9 mm^3 in the lateral, axial and elevation dimensions, respectively, at 50 V. The beam profiles and 2D scan of the focal region are shown in Figure 3. The PNP as a function of the applied voltage is shown in Figure 4. The presence of two peaks in elevation (Figure 3) is caused by the hydrophone placement closer to the transducer surface than the elevation focus of the acoustic lens. Applying 90 V resulted in the highest estimated PNP of 4.4 MPa with intensities of I_{sptp} = 1300 W/cm^2 and I_{satp} = 515 W/cm^2. Here I_{sptp} and I_{satp} are spatial peak temporal peak and spatial average temporal peak intensity, respectively. Applying 70 V resulted in estimated PNP of 3.4 MPa with intensities of I_{sptp} = 775 W/cm^2 and I_{satp} = 320 W/cm^2. The PRF of 1 Hz was used for the intensity calculations.

Microbubbles

The measured concentration and size range (mean and median diameters) of the four microbubble types are shown in Table 2. MicroMarker microbubbles were the most visible contrast agent in all tissues in the frequency range used with the Verasonics Vantage 256 scanner and L11–5 probe. BR38 were visible mostly in normal tissues but were rarely visible inside the tumor, while Definity and Sonovue were not well visualized in any tissue. CEUS images of the HCC tumors with different microbubbles are shown in Figure 5. Based on its visibility in the animal model, MicroMarker was selected for the remaining studies (i.e. in therapeutic ultrasound parameter optimization and *in vivo*-optimized vs. phantom-optimized studies).

Ultrasound Parameter Optimization

PRF and Voltage—An example of the measured and fitted time-intensity curves after applying a single 90 V therapeutic US pulse is shown in Figure 6, for which the estimated t_p using Equation 1 was 1.51 ± 0.11 sec. The time-intensity curves for different applied voltages are shown in Figure 7. The mean values for the perfusion time were 0.9 ± 0.9 sec and 1.9 ± 0.9 sec for therapeutic US pulses of 70 V and 90 V, respectively. The time-intensity curves for the same focal region after applying the 1-st and 100-th therapeutic pulses are shown in Figure 7 (e, f). The mean perfusion time for the experiments with up to 100 therapeutic pulses at 90 V, applied to the same focal region, was 2.1 ± 0.7 sec. Thus, the PRF_{opt} should be selected to be approximately 1 Hz or 0.5 Hz if applying a therapeutic pulse of 70 V or 90 V, respectively (see Equation 2).

Treatment Time—IF images of the HCC tumors treated for 10, 30, 50, 75, and 100 sec with PRF_{opt} = 1 Hz and PNP of 3.4 MPa (70 V applied voltage) are shown in Figure 8. The mean value of SPN channel intensity per unit vessel area is shown in Figure 9. The US therapies with 75 and 100 pulses delivered 4.7 (p = 0.0158) and 5.9 (p = 0.0007) times more SPNs than the therapy with 10 pulses, respectively.

Comparison of in vivo-Optimized and Phantom-Optimized Parameters—The selected optimal parameters for the USMB mediated therapy comparison study are shown in Table 3. The IF images of the *in vivo*-optimized, phantom-optimized, and control mice tumors are shown in Figure 10. There were no significant differences in SPN penetration depth between the therapies. The mean SPN penetration depth was 11 ± 6 μm and 13 ± 7 μm for the therapies with *in vivo*-optimized and phantom-optimized US parameters, respectively (Figure 11, left). The total fold increase for the tumors treated with *in vivo*-optimized or optimized US parameters compared to the non-treated tumor increased from 1.4 ± 0.7 (phantom-optimized) to 3.0 ± 0.8 (*in vivo*-optimized) for the SPN intensity normalized by the vessel area, and from 1.3 ± 0.5 (phantom-optimized) to 2.8 ± 0.7 (*in vivo*-optimized) for the SPN intensity normalized by the vessel length ($p < 0.01$) (Figure 11, right). In addition, therapy with *in vivo*-optimized US parameters had a significant increase in both vessel area and vessel length normalized SPN intensity compared to control ($p < 0.01$). The phantom-optimized US therapy parameters showed a significant increase in SPN delivery ($p < 0.05$) compared to the control when normalized to the vessel area but not the vessel length.

H&E stained tumor sections showed no tissue damage in animals with US treatments of various acoustic parameters, compared to the control tumor tissue sections without US treatment (Figure 12).

Discussion

An *in vivo* US parameter optimization study was carried out to assess the difference between phantom and *in vivo* optimization of US therapy parameters. Typically, phantom optimization studies have a vessel with a controlled diameter (usually in the range of a few millimeters), high microbubble concentration, and a uniform microbubble flow rate. *In vivo*, the microvasculature has diameters on the order of tens of microns, low microbubble concentration due to the blood dilution, low microbubble stability, and complex perfusion.

The microbubble backscattering signal strength depends on multiple parameters, including microbubble size, gas core, shell stiffness, ultrasound frequency, and proximity of the vessel walls among other factors. In CEUS images, the MicroMarker microbubbles were the most visible among the other microbubbles used in this study and were selected to be the primary microbubbles for the remaining studies. A potential source of error in selecting the most visible microbubble type was the lack of concentration-normalized doses of the used microbubbles. In addition, the manufacturer recommended MB activation protocols and concentrations were used. Microbubbles are complex structures with different shell and inner gas properties finely tuned to achieve a strong non-linear response at diagnostic frequencies. Because MicroMarker microbubbles are designed to achieve strong acoustic response at high frequencies (Sun et al., 2014), it is possible that other microbubbles may perform better at lower frequencies than those used in this study.

The measured perfusion time for 90 V (MI = 1.54, $t_p = 1.9$ sec) therapeutic pulses was approximately twice as large as that for 70 V (MI = 1.22, $t_p = 0.9$ sec). Assuming that inertial cavitation was induced only for microbubbles inside the sonicated volume with MI greater than 0.6 (Datta et al., 2006), the cavitation volume would be 16.0 and 36.8 mm^3 for

70 V and 90 V, respectively. Thus, a relatively small increase of MI from 1.22 to 1.54 results in doubling the cavitation volume within the tumor, resulting in a significant difference in perfusion time. To minimize the treatment time and ensure optimal concentration of microbubbles in the tumor site, 1 Hz PRF and 70 V were selected as optimal therapeutic US parameters.

Because inertial cavitation is capable of damaging blood vessels, it is possible that the vessels could become leaky after multiple therapeutic US pulses delivered to the same region, resulting in variations of the perfusion time. To test this hypothesis, the perfusion time was measured every 10 therapeutic pulses applied to the same therapy region. Because there was no significant difference in the measured t_p values after the 1st and 100th pulses, we conclude that there was no vascular damage from IC. The lack of vascular damage is confirmed in our H&E stains (Figure 12).

Applying therapy for a short period of time is inadvisable due to low drug delivery rate, while overtreatment will result in diminishing returns and unnecessary long treatment time. The 4.7 ($p = 0.0158$) to 5.9 ($p = 0.0007$) fold increase of the delivered SPNs was observed if therapy time was increased from 10 to 75 and 100 seconds, respectively. This showed that longer therapy time resulted in a larger amount of successfully delivered SPNs, but the longest therapy time did not result in a significant increase in delivery compared to 75 sec therapy.

The SPN penetration depth was similar between the *in vivo*-optimized and phantom-optimized US parameters due to the small difference in MI values used in this study (Wang et al., 2015). However, the overall control-normalized intensity of the SPN signal in the HCC tumor was up to 2.2 fold higher for the mice treated with *in vivo*-optimized US parameters compared to those treated with phantom-optimized US parameters (Figure 11). The increase in the total amount of SPNs was significant ($p < 0.01$) for both area- and length-normalized intensity values.

Inertial cavitation of microbubbles leads to sonoporation and increased drug delivery, making the presence of microbubbles in the treatment area crucial. After the injection of microbubbles and the model nanocarrier (SPNs in this study), the first US therapy pulse is efficient at delivering drug because there is a high microbubble concentration in the target region. However, the microbubbles will be destroyed due to inertial cavitation. In order to make all consecutive therapeutic pulses as efficient as the first one, a similar microbubble concentration is required in the therapy region throughout the whole treatment time. To achieve this, the time delay between two consecutive therapeutic pulses should be high enough to allow microbubbles to perfuse from the surrounding blood vessels back into the target region. The delay between therapy pulses should be no shorter than the perfusion time t_p. Thus, we show that having a PRF optimized to the tumor's vascular dynamics is the main reason for the increased drug delivery compared to tumors having phantom optimized US parameters.

To simplify the translation to potential human applications, we replaced our previous dual-transducer design (Chowdhury et al., 2016, 2018) with a single-transducer design (Figure 1).

This eliminated problems associated with transducer alignment, coupling, and a limited field of view due to the imaging transducer positioned relative to therapy transducer. However, the main shortcoming of the single transducer design is that the transducer has a limited bandwidth for imaging and therapy. Thereby, using a single-transducer setup and driving the L11–5 transducer at a central frequency of 7.8 MHz resulted in MI values significantly lower than those used in our previous studies (Wang et al., 2015; Chowdhury et al., 2016, 2018). This low MI resulted in a reduced penetration depth of the SPNs into the tumors (Wang et al., 2015). One of the possible ways to increase MI is to use a lower frequency transducer. No comparison of the *in vivo*-optimized therapy used in this study with the therapy using the dual-transducer design (Chowdhury et al., 2016, 2018) has been carried out.

A limitation of our study is that a total of 30 mice were used for all experiments, including optimization of voltage, PRF, and treatment time, and for comparing drug delivery efficiency of *in vivo* optimized and phantom-optimized therapeutic US parameters. Because these mice were split into multiple groups, a small number of mice per group were utilized for several of the experiments, thereby decreasing the power of our individual experiments. Nevertheless, this pilot study suggests that optimization of therapeutic US parameters to the specific task, experiment, or model could significantly improve the efficiency of USMB-mediated drug delivery.

In vivo optimization of therapeutic US parameters led to significant improvement of drug delivery to the HCC model in mice. Similar optimization studies may be beneficial when using such a USMB drug-delivery platform in clinical applications, but *ex vivo* histology analysis in humans would be impractical. However, the PRF could be optimized on a patient-by-patient basis by estimating the perfusion time during the initial USMB injection via the time-intensity curves approach used herein. In addition, the human liver is located relatively deep within the abdominal cavity. Based on these results, we anticipate that maximizing MI and aiming for treatment time based on pre-clinical studies in large animals would be the most appropriate optimization for clinical application.

Conclusions

We have shown that *in vivo* optimization of therapeutic US parameters, such as PRF, voltage, and treatment time improves the efficiency of drug delivery to tumors. We showed that, for our system, the most efficient drug delivery in a subcutaneous mouse model of HCC was obtained using 70 V voltage (MI 1.22), 1 Hz PRF, and 100 sec treatment time (100 pulses per therapy region). Those mice that received therapy using optimized US parameters showed up to a 2.2 increase ($p < 0.01$) in drug delivered to the HCC tumor compared to therapy with phantom-optimized US parameters. We believe the improvement in drug delivery is primarily achieved by using a relatively low PRF, which ensures high microbubble concentration in the target region prior to each and every therapeutic US pulse.

Acknowledgements

The authors would like to acknowledge Drs. Dongwoon Hyun and Taehwa Lee from Stanford University, Department of Radiology, for their help with the study. The work was supported by the National Institutes of Health, grant numbers R01CA209888 and R21EB022298.

References

Averkiou M, Powers J, Skyba D, Bruce M, Jensen S, 2003. Ultrasound contrast imaging research. Ultrasound Q. 19 (1), 27–37. [PubMed: 12970614]

Babakhanian M, Yang L, Nowroozi B, Saddik G, Boodaghians L, Blount P, Grundfest W, 2018. Effects of low intensity focused ultrasound on liposomes containing channel proteins. Scientific reports8 (1), 1–9. [PubMed: 29311619]

Bao L, Yan Y, Xu C, Ji W, Shen S, Xu G, Zeng Y, Sun B, Qian H, Chen L, Wu M, Su C, Chen J, 2013. MicroRNA-21 suppresses PTEN and hSulf-1 expression and promotes hepatocellular carcinoma progression through AKT/ERK pathor2. Cancer Lett. 337 (2), 226–236. [PubMed: 23684551]

Bao S, Thrall BD, Miller DL, 1997. Transfection of a reporter plasmid into cultured cells by sonoporation *in vitro*. Ultrasound Med. Biol. 23 (6), 953–959. [PubMed: 9300999]

Belghiti J, Panis Y, Farges O, Benhamou J, Fekete F, 1991. Intrahepatic recurrence after resection of hepatocellular carcinoma complicating cirrhosis. Ann. Surg. 214 (2), 114–117. [PubMed: 1714267]

Bismuth H, Chiche L, Adam R, Castaing D, Diamond T, Dennison A, 1993. Liver resection versus transplantation for hepatocellular carcinoma in cirrhotic patients. Ann. Surg. 218 (2), 145–151. [PubMed: 8393649]

Camm C, Schepis F, Orlando A, Albanese M, Shahied L, Trevisani F, Andreone P, Crax A, Cottone M, 2002. Transarterial chemoembolization for unresectable hepatocellular carcinoma: Meta-analysis of randomized control. trials. Radiol. 224 (1), 47–54.

Chowdhury SM, Lee T, Bachawal SV, Devulapally R, Abou-Elkacem L, Yeung TA, Wischhusen J, Tian L, Dahl J, Paulmurugan R, Willmann JK, 2018. Longitudinal assessment of ultrasound-guided complementary microRNA therapy of hepatocellular carcinoma. J. of Control. Release281, 19–28. [PubMed: 29758233]

Chowdhury SM, Wang T-Y, Bachawal S, Devulapally R, Choe JW, Elkacem LA, Yakub BK, Wang DS, Tian L, Paulmurugan R, Willmann JK, 2016. Ultrasound-guided therapeutic modulation of hepatocellular carcinoma using complementary microRNAs. J. of Control. Release238, 272–280. [PubMed: 27503707]

Couture O, Bannouf S, Montaldo G, Aubry J-F, Fink M, Tanter M, 2009. Ultrafast imaging of ultrasound contrast agents. Ultrasound Med. Biol. 35 (11), 1908–1916. [PubMed: 19699026]

Couture O, Fink M, Tanter M, 2012. Ultrasound contrast plane wave imaging. IEEE Trans. Ultrason. Ferroelec., Freq. Contr. 59 (12), 2676–2683.

Datta S, Coussios C-C, McAdory LE, Tan J, Porter T, Courten-Myers GD, Holland CK, 2006. Correlation of cavitation with ultrasound enhancement of thrombolysis. Ultrasound Med. Biol. 32 (8), 1257–1267. [PubMed: 16875959]

Eggen S, Afadzi M, Nilssen E, Haugstad S, Angelsen B, de L. Davies C, 2013. Ultrasound improves the uptake and distribution of liposomal doxorubicin in prostate cancer xenografts. Ultrasound Med. Biol. 39 (7), 1255–1266. [PubMed: 23643054]

Eggen S, Fagerland S-M, rr Mrch, Hansen R, Svik K, Berg S, Furu H, Bhn AD, Lilledahl MB, Angelsen A, Angelsen B, de Lange Davies C, 2014. Ultrasound-enhanced drug delivery in prostate cancer xenografts by nanoparticles stabilizing microbubbles. J. of Control. Release187, 39–49. [PubMed: 24852099]

Ercolani G, Grazi G, Ravaioli M, Del Gaudio M, Gardini A, Cescon M, Varotti G, Cetta F, Cavallari A, 2003. Liver resection for hepatocellular carcinoma on cirrhosis: Univariate and multivariate analysis of risk factors for intrahepatic recurrence. Ann. Surg. 237 (4), 536–543. [PubMed: 12677151]

European Association for the Study of the Liver and European Organisation for Research and Treatment of Cancer, 2012. EASL-EORTC clinical practice guidelines: Management of hepatocellular carcinoma. J. of Hepatol. 56 (4), 908–943. [PubMed: 22424438]

Fattovich G, Stroffolini T, Zagni I, Donato F, 2004. Hepatocellular carcinoma in cirrhosis: Incidence and risk factors. Gastroenterol. 127 (5, Supplement 1), S35–S50.

Forner A, Reig M, Bruix J, 2018. Hepatocellular carcinoma. Lancet391 (10127), 1301–1314. [PubMed: 29307467]

Gerber H-P, Senter PD, Grewal IS, 2009. Antibody drug-conjugates targeting the tumor vasculature. mAbs1 (3), 247–253. [PubMed: 20069754]

Grolami R, Uch R, Brchot C, Mannoni P, Bagnis C, 2003. Gene therapy of hepatocarcinoma: a long way from the concept to the therapeutical impact. Cancer Gene Ther. 10, 649–660. [PubMed: 12944984]

Hsu S-H, Wang B, Kota J, Yu J, Costinean S, Kutay H, Yu L, Bai S, Perle K, Chivukula R, Mao H, Wei M, Clark K, Mendell J, Caligiuri M, Jacob S, Mendell J, Ghoshal K, 2012. Essential metabolic, anti-inflammatory, and anti-tumorigenic functions of miR-122 in liver. J. Clin. Investig. 122 (8), 2871–2883. [PubMed: 22820288]

Hyun D, Abou-Elkacem L, Perez VA, Chowdhury SM, Willmann JK, Dahl JJ, 2018. Improved sensitivity in ultrasound molecular imaging with coherence-based beamforming. IEEE Transactions on Medical Imaging37 (1), 241–250. [PubMed: 29293430]

Ianni TD, Bose RJ, Sukumar UK, Bachawal S, Wang H, Telichko A, Herickhoff C, Robinson E, Baker S, Vilches-Moure JG, Felt SA, Gambhir SS, Paulmurugan R, Dahl JD, 2019. Ultrasound/microbubble-mediated targeted delivery of anticancer microRNA-loaded nanoparticles to deep tissues in pigs. J. of Control. Release309, 1–10. [PubMed: 31326463]

Jopling C, 2012. Liver-specific microRNA-122: Biogenesis and function. RNA Biology9 (2), 137–142. [PubMed: 22258222]

Kurdziel KA, Kalen JD, Hirsch JI, Wilson JD, Bear HD, Logan J, McCumisky J, Moorman-Sykes K, Adler S, Choyke PL, 2011. Human dosimetry and preliminary tumor distribution of 18f-fluoropaclitaxel in healthy volunteers and newly diagnosed breast cancer patients using PET/CT. J. Nucl. Med. 52 (9), 1339–1345. [PubMed: 21849404]

Lai C-Y, Fite BZ, Ferrara KW, 2013. Ultrasonic enhancement of drug penetration in solid tumors. Frontiers Oncol. 3, 204.

Lau W, Lai E, 2007. Salvage surgery following downstaging of unresectable hepatocellular carcinoma - a strategy to increase resectability. Ann. Surg. Oncol. 14 (12), 3301–3309. [PubMed: 17891443]

Lencioni R, Petruzzi P, Crocetti L, 2013. Chemoembolization of hepatocellular carcinoma. Seminars Interventional Radiol. 30 (1), 3–11.

Llovet JM, Schwartz M, Mazzaferro V, 2005. Resection and liver transplantation for hepatocellular carcinoma. Seminars Liver Dis. 25 (2), 181–200.

Lo C-M, Ngan H, Tso W-K, Liu C-L, Lam C-M, Poon RT-P, Fan S-T, Wong J, 2002. Randomized control. trial of transarterial lipiodol chemoembolization for unresectable hepatocellular carcinoma. Hepatol. 35 (5), 1164–1171.

Mazzaferro V, Bhoori S, Sposito C, Bongini M, Langer M, Miceli R, Mariani L, 2011. Milan criteria in liver transplantation for hepatocellular carcinoma: An evidence-based analysis of 15 years of experience. Liver Transplant. 17 (S2), S44–S57.

Mazzaferro V, Regalia E, Doci R, Andreola S, Pulvirenti A, Bozzetti F, Montalto F, Ammatuna M, Morabito A, Gennari L, 1996. Liver transplantation for the treatment of small hepatocellular carcinomas in patients with cirrhosis. New Engl. J. Med. 334 (11), 693–700. [PubMed: 8594428]

Michel J, Suc B, Montpeyroux F, Hachemanne S, Blanc P, Domergue J, Mouiel J, Gouillat C, Ducerf C, Saric J, Treut YPL, Fourtanier G, Escat J, 1997. Liver resection of transplantation for hepatocellular carcinoma? Restrospective analysis of 215 patients with cirrhosis. J. Hepatol. 26 (6), 1274–1280. [PubMed: 9210614]

Miller DL, Quddus J, 2000. Diagnostic ultrasound activation of contrast agent gas bodies induces capillary rupture in mice. Proceedings of the National Academy of Sciences97 (18), 10179–10184.

Mittal S, El-Serag HB, 2013. Epidemiology of hepatocellular carcinoma: consider the population. J. Clin. gastroenterol. 47, S2–6. [PubMed: 23632345]

Murata S, Mine T, Ueda T, Nakazawa K, Onozawa S, Yasui D., i.Kumita S, 2013. Transcatheter arterial chemoembolization based on hepatic hemodynamics for hepatocellular carcinoma. The Scientific World J, 479805–1–8.

Njei B, Rotman Y, Ditah I, Lim JK, 2015. Emerging trends in hepatocellular carcinoma incidence and mortality. Hepatol. 61 (1), 191–199.

Pu K, Shuhendler AJ, Valta MP, Cui L, Saar M, Peehl DM, Rao J, 2014. Phosphorylcholine-coated semiconducting polymer nanoparticles as rapid and efficient labeling agents for in vivo cell tracking. Adv. Healthc. Mater. 3 (8), 1292–1298. [PubMed: 24668903]

Simard EP, Ward EM, Siegel R, Jemal A, 2012. Cancers with increasing incidence trends in the United States: 1999 through 2008. CA: Cancer J. Clin. 62 (2), 118–128. [PubMed: 22281605]

Snipstad S, Berg S, rr Mrch, Bjrky A, Sulheim E, Hansen R, Grimstad I, van Wamel A, Maaland AF, Torp SH, de Lange Davies C, 2017. Ultrasound improves the delivery and therapeutic effect of nanoparticle-stabilized microbubbles in breast cancer xenografts. Ultrasound Med. Biol. 43 (11), 2651–2669. [PubMed: 28781149]

Sun C, Sboros V, Butler M, Moran C, 2014. *In vitro* acoustic characterization of three phospholipid ultrasound contrast agents from 12 to 43 MHz. Ultrasound Med. Biol. 40 (3), 541–550. [PubMed: 24361219]

Tomimaru Y, Eguchi H, Nagano H, Wada H, Kobayashi S, Marubashi S, Tanemura M, Tomokuni A, Takemasa I, Umeshita K, Kanto T, Doki Y, Mori M, 2012. Circulating microRNA-21 as a novel biomarker for hepatocellular carcinoma. J. of Hepatol. 56 (1), 167–175. [PubMed: 21749846]

Tsai W-C, Hsu S-D, Hsu C-S, Lai T-C, Chen S-J, Shen R, Huang Y, Chen H-C, Lee C-H, Tsai T-F, Hsu M-T, Wu J-C, Huang H-D, Shiao M-S, Hsiao M, Tsou A-P, 2012. MicroRNA-122 plays a critical role in liver homeostasis and hepatocarcinogenesis. J. of Clin. Investig. 122 (8), 2884–2897. [PubMed: 22820290]

Vignon F, Shi W, Powers J, Everbach E, Liu J, Gao S, Xie F, Porter T, 2013. Microbubble cavitation imaging. IEEE Trans. Ultrason. Ferroelec., Freq. Contr. 60 (4), 661–670.

Vogel A, Cervantes A, Chau I, Daniele B, Llovet J, Meyer T, Nault J, Neumann U, Ricke J, Sangro B, Schirmacher P, Verslype C, Zech C, Arnold D, Martinelli E, ESMO Guidelines Committee, 2018. Hepatocellular carcinoma: ESMO clinical practice guidelines for diagnosis, treatment and follow-up. Ann. Oncol. 29 (Suppl. 4), iv238–iv255. [PubMed: 30285213]

Wang T-Y, Choe J, Pu K, Devulapally R, Bachawal S, Machtaler S, Chowdhury S, Luong R, Tian L, Khuri-Yakub B, Rao J, Paulmurugan R, Willmann JK, 2015. Ultrasound-guided delivery of microRNA loaded nanoparticles into cancer. J. of Control. Release203, 99–108. [PubMed: 25687306]

Wu C, Chiu D, 2013. Highly fluorescent semiconducting polymer dots for biology and medicine. Angewandte Chemie - Int. Edition52 (11), 3086–3109.

Xu J, Zhu X, Wu L, Yang R, Yang Z, Wang Q, Wu F, 2012. MicroRNA-122 suppresses cell proliferation and induces cell apoptosis in hepatocellular carcinoma by directly targeting Wnt/β-catenin pathway. Liver Int. 32 (5), 752–760. [PubMed: 22276989]

Xu Y, Xia F, Ma L, Shan J, Shen J, Yang Z, Liu J, Cui Y, Bian X, Bie P, Qian C, 2011. MicroRNA-122 sensitizes HCC cancer cells to adriamycin and vincristine through modulating expression of mdr and inducing cell cycle arrest. Cancer Lett. 310 (2), 160–169. [PubMed: 21802841]

Zhou Y, Wang Y-N, Farr N, Zia J, Chen H, Ko BM, Khokhlova T, Li T, Hwang JH, 2016. Enhancement of small molecule delivery by pulsed-high intensity focused ultrasound (pHIFU): A parameter exploration. Ultrasound Med. Biol. 42 (4), 956–963. [PubMed: 26803389]

Zhu Q, Wang Z, Hu Y, Li J, Li X, Zhou L, Huang Y, 2012. miR-21 promotes migration and invasion by the miR-21-PDCD4-AP-1 feedback loop in human hepatocellular carcinoma. Oncol. Rep. 27 (5), 1660–1668. [PubMed: 22322403]

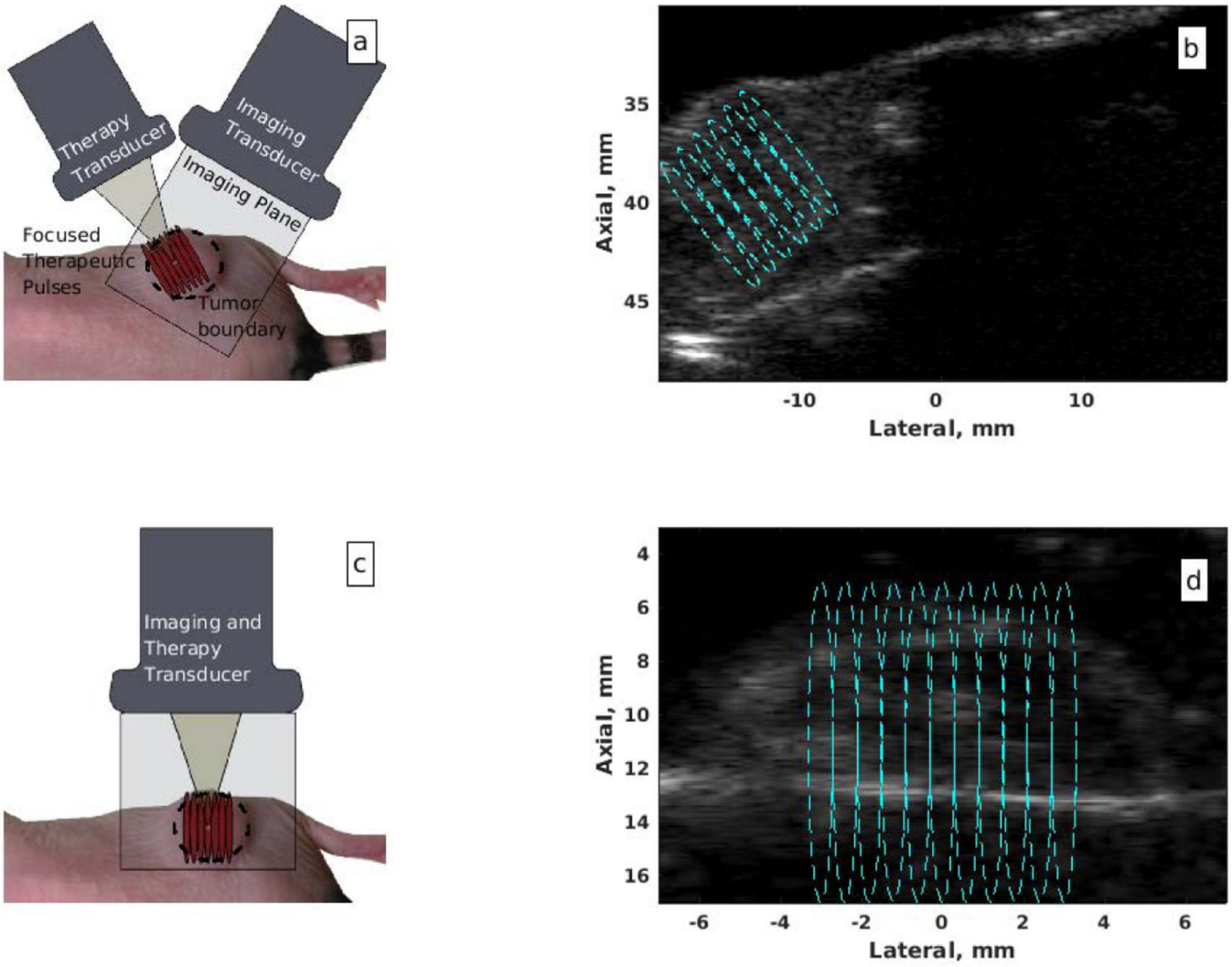

Figure 1:
US-mediated drug-delivery system: (a) dual-transducer design used in (Chowdhury et al., 2016, 2018), and (b) corresponding B-mode image. (c) Single transducer design, used in this study, and (d) corresponding B-mode image.

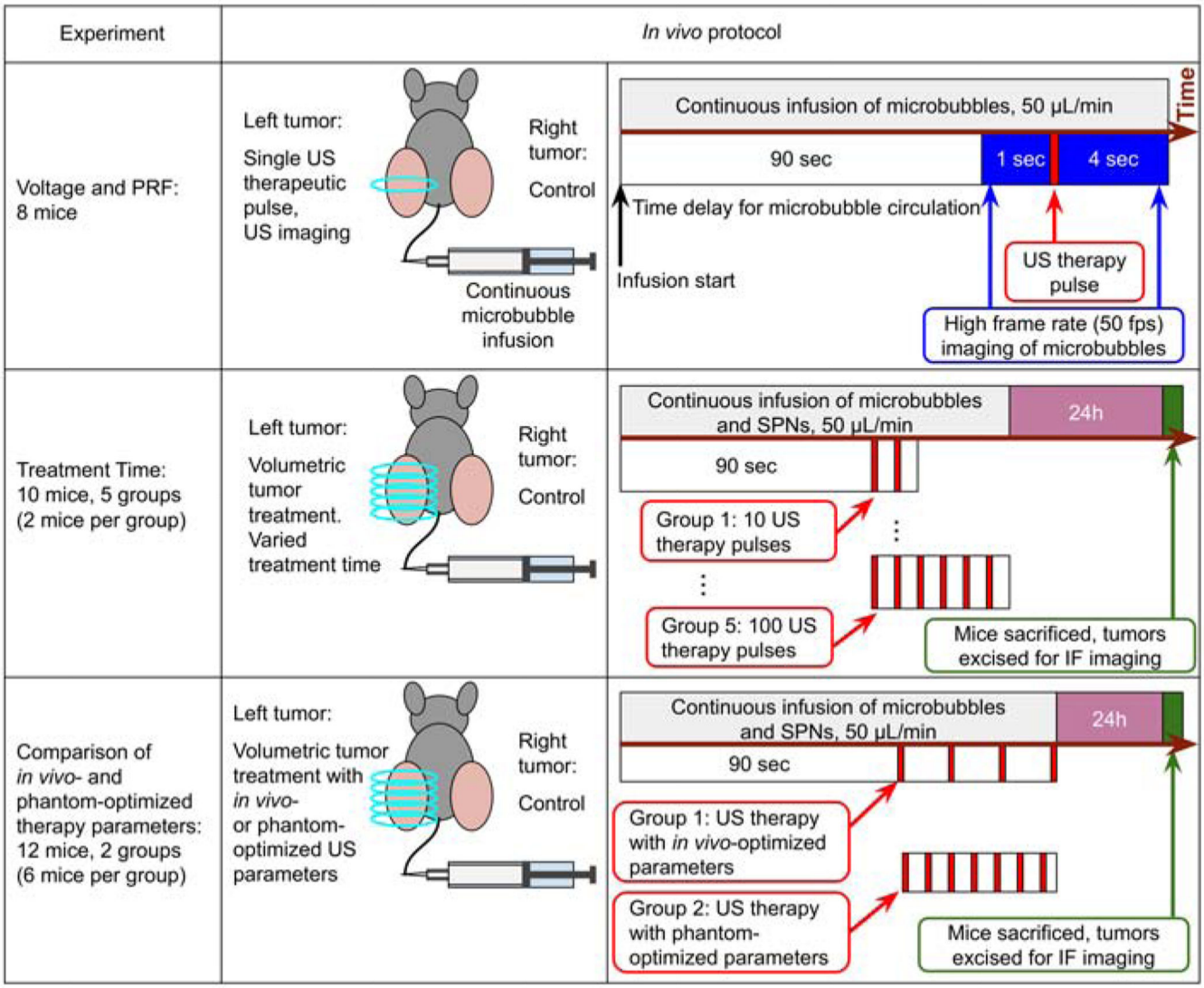

Figure 2:

Schematic view of the *in vivo* US parameter optimization experiments. Top row: PRF and voltage parameter optimization experiments. CEUS image intensity was used to determine the optimal PRF and voltage. Middle row: Treatment time optimization experiments. Confocal immunofluorescence imaging was used to determine the optimal number of pulses per focal region. Bottom row: Comparison of *in vivo*-optimized and phantom-optimized therapy parameters experiments. Confocal immunofluorescence imaging used to determine the therapy resulting in higher SPN delivery to the HCC tumor.

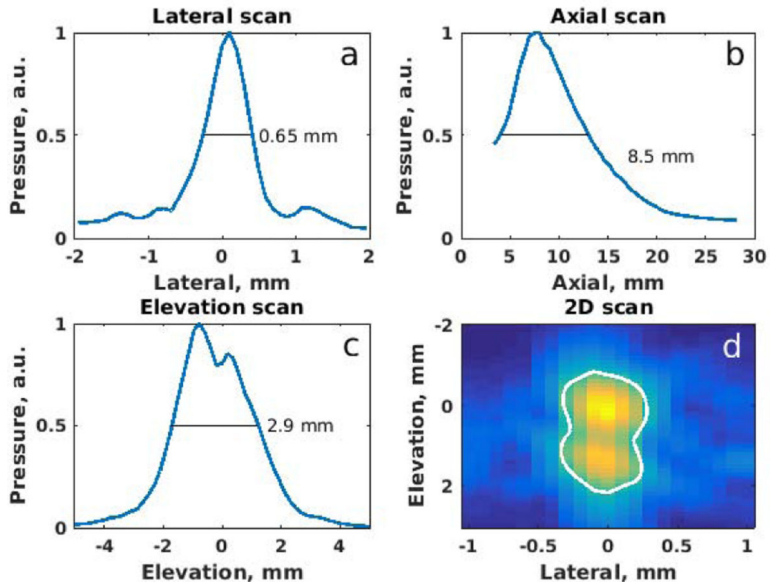

Figure 3:

Measured therapy beam's profile. a) Lateral scan; b) axial scan; c) elevation scan; d) 2D lateral/elevation scan with −6 dB area contour shown in white.

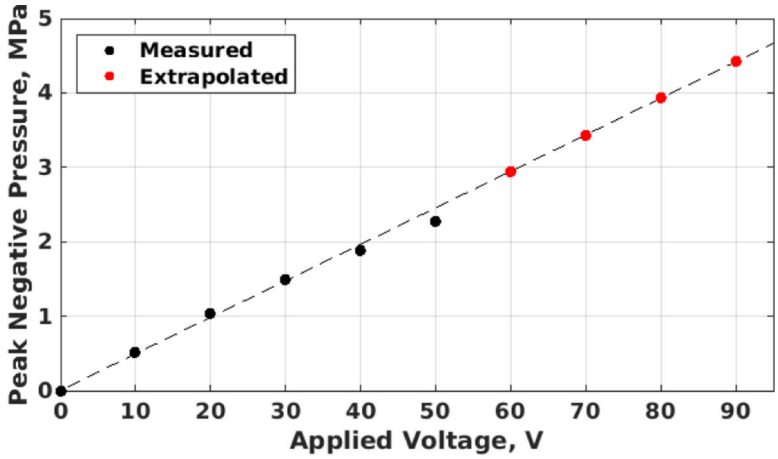

Figure 4:

Peak negative pressure in water as a function of applied voltage for the focused excitation from the L11-5 transducer.

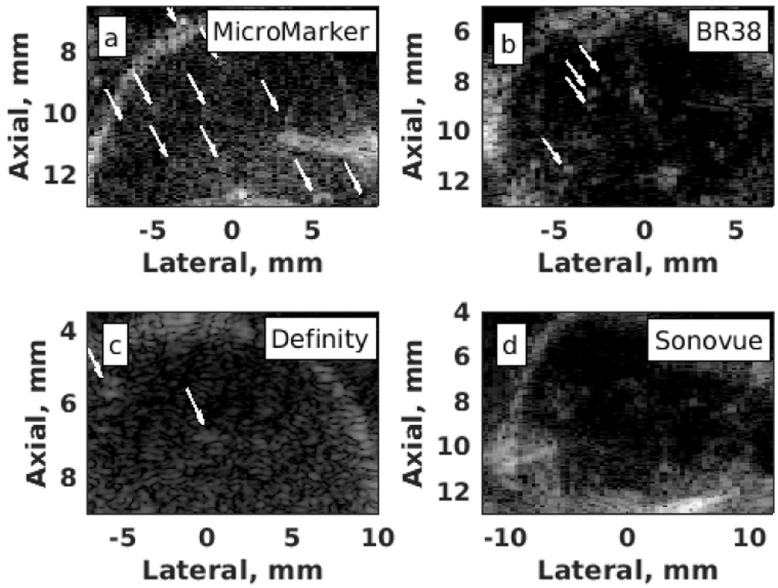

Figure 5:

CEUS images of HCC tumor in mice injected with different microbubbles: a) MicroMarker; b) BR38; c) Definity d) Sonovue. White arrows indicate the location of visible microbubbles. All images show 50 dB of dynamic range.

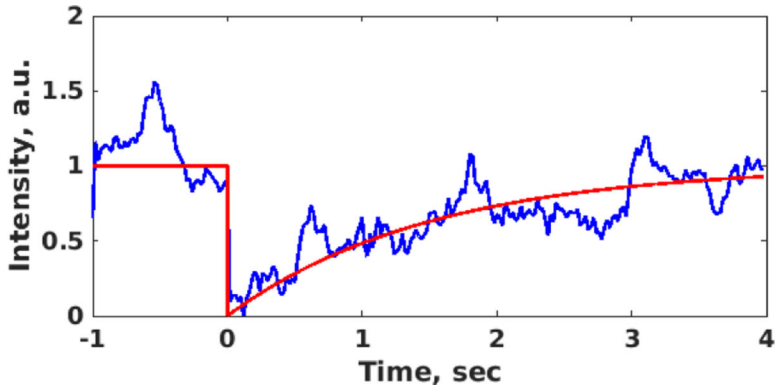

Figure 6:

Experimentally obtained (blue) and fitted (red) time-intensity curves after applying a therapeutic US pulse of 90 V. The time-intensity curve measured here was t_p = 1.51 ± 0.11 sec, yielding a PRF of ~0.7 Hz.

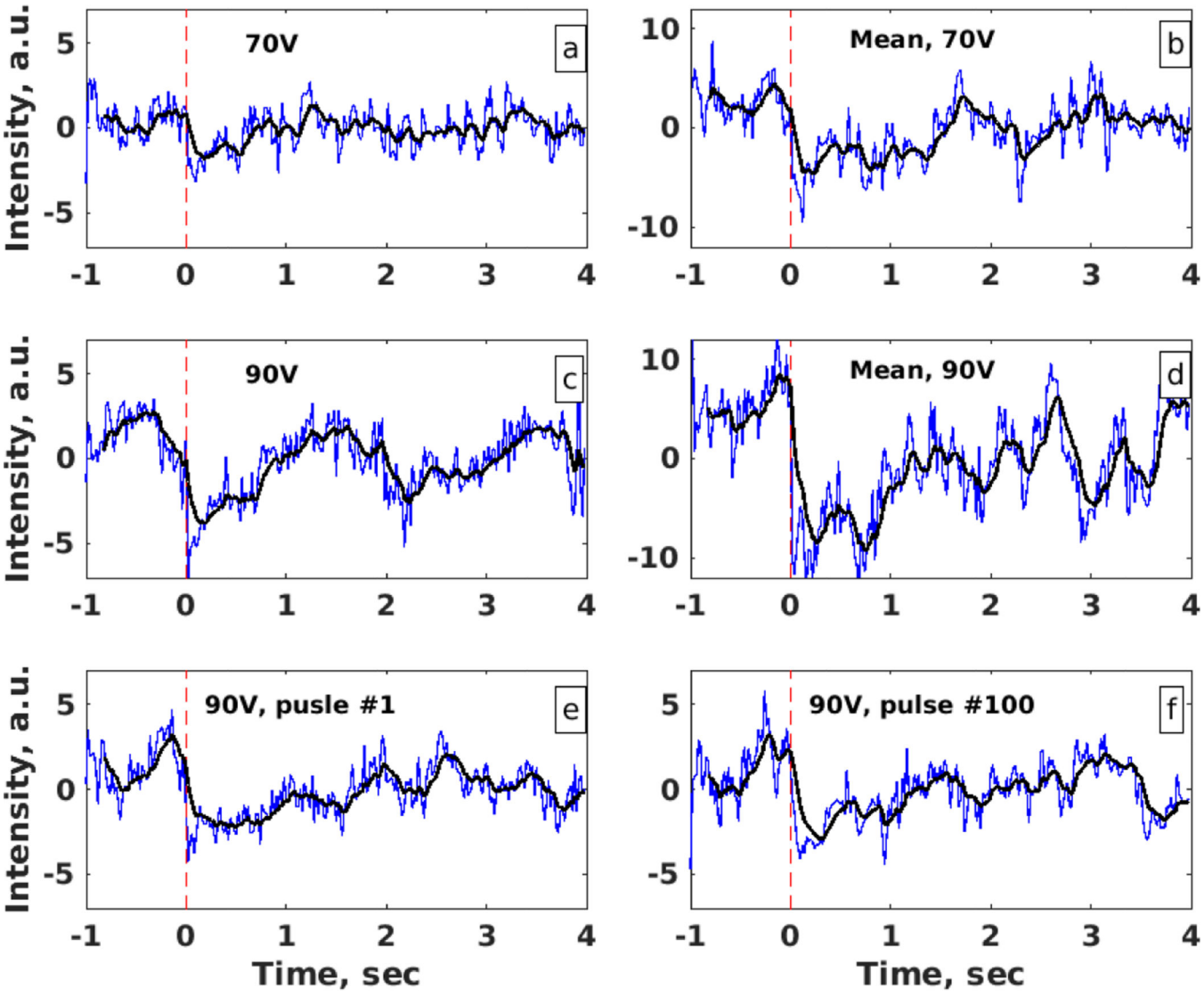

Figure 7:

Measured time-intensity curves (blue) and their running average (black) in HCC tumors after: (a) applying a single therapeutic US pulse (red dashed line) at 70 V; (b) average curve for all experiments at 70 V; (c) applying a single therapeutic US pulse at 90 V; (d) average curve for all experiments at 90 V; (e) first pulse at 90 V; (f) 100th pulse at 90 V applied to the same focal region as in (e).

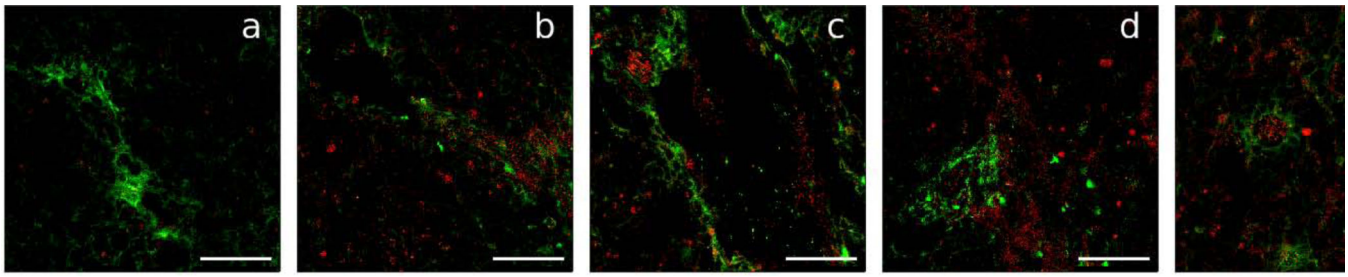

Figure 8:

Representative immunofluorescence images of SPN model drug (red) and endothelial marker CD31 (green) for blood vessel visualization in subcutaneous HCC tumors. The tumors were treated with *in vivo*-optimized PRF (1 Hz) and voltage (70 V, MI = 1.22), while the therapy time was varied: (a) 10 sec; (b) 30 sec; (c) 50 sec; (d) 75 sec; (e) 100 sec. Scale bars are 75 μm.

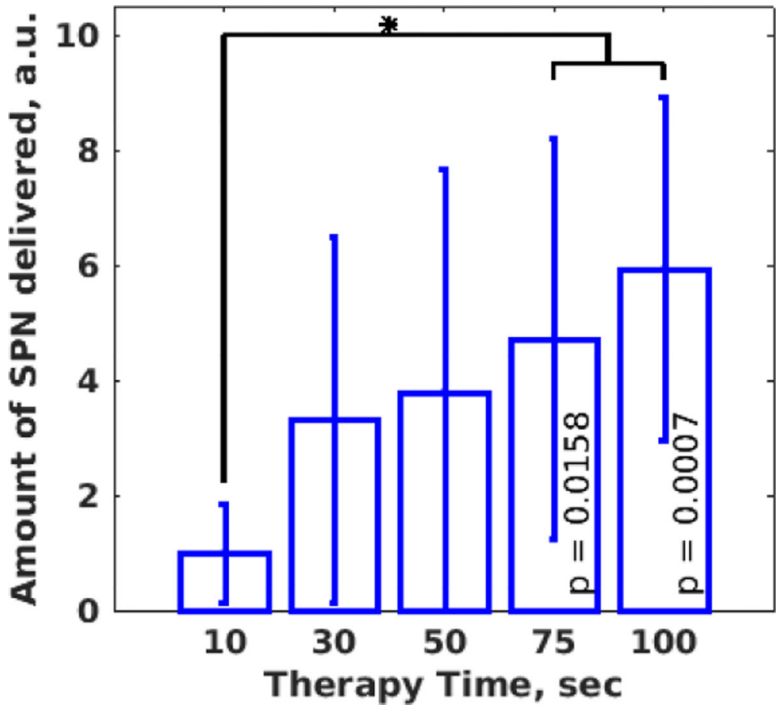

Figure 9:

Amount of SPN (per unit vessel area, normalized to 10 pulses) delivered to the HCC tumor cells after applying US therapy with *in vivo*-optimized PRF_{opt} (1 Hz) and voltage (70 V, MI = 1.22) and varying treatment time. Error bars represent the standard deviation from the mean value.

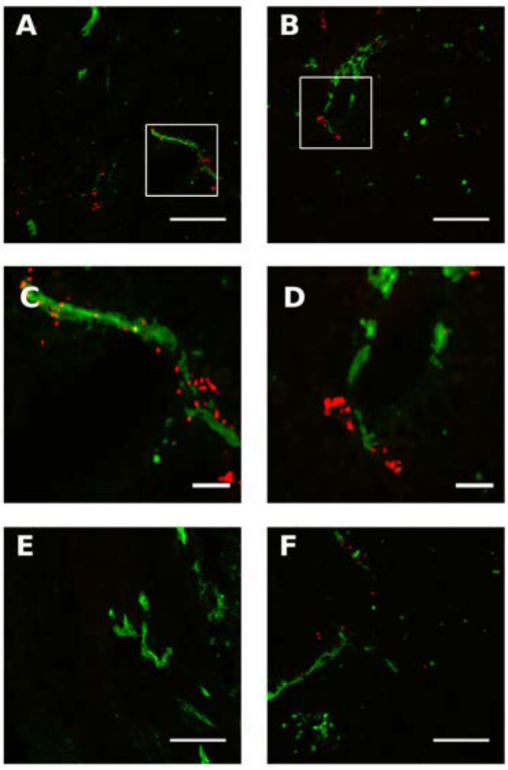

Figure 10:

Representative immunofluorescence images of SPN model drug (red) and endothelial marker CD31 (green) for blood vessel visualization in subcutaneous HCC tumors. (a) treated region with *in vivo*-optimized US parameters; (b) treated region with phantom-optimized US parameters; (c) magnification of a region inside the square in (a); (d) magnification of a region inside the square in (b); (e) untreated region in the control tumor, same mouse as in (a); (f) untreated region in the control tumor, same mouse as in (b). Scale bars are 100 μm in (a), (b), (d), (e), and 20 μm in (c), (d).

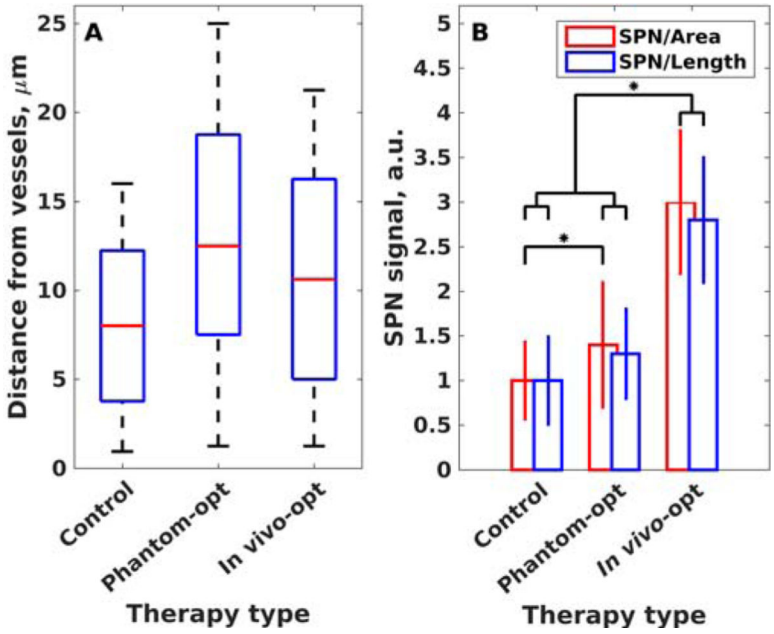

Figure 11:

Comparison of therapy using phantom-optimized and *in vivo*-optimized parameters. Left: SPN penetration depth from blood vessels into tumor. The central mark indicates the median, and the edges of the box indicate interquartile range. There was no significant difference between the control tumors or those treated with *in vivo* optimized US parameters. Right: Quantification of the control-normalized increase in the SPN intensity for therapies using *in vivo*-optimized and phantom-optimized parameters. Error bars represent the standard deviation from the mean value.

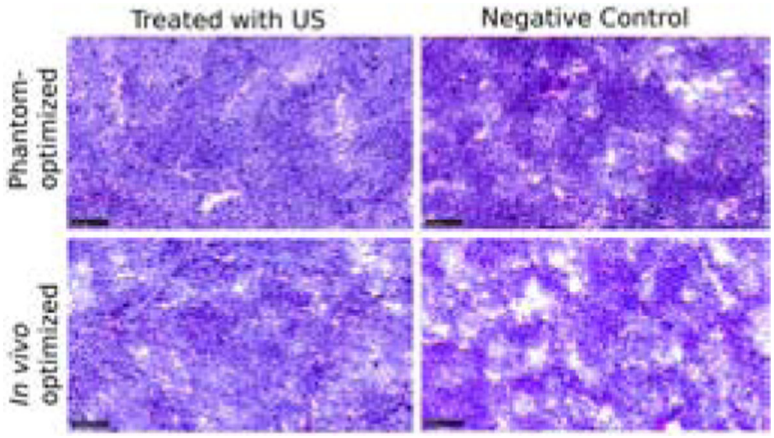

Figure 12:

Representative H&E-stained tumor sections in treated groups with phantom-optimized or *in vivo*-optimized US acoustic parameters show no histological damage compared to the control tumors without US treatment. Scale bar, 100 μm.

[Table 1:]

Fixed Ultrasound Parameters for Imaging and Therapy.

	Imaging	**Therapy**
Frequency, MHz	5 (TX), 10 (Receive)	7.8
US excitation type	Plane wave synthetic aperture	focused
No of US cycles	1	25
Focal depth, mm	n/a	8
No of areas/planes	25 planes (−10° … 10°)	11 areas

[Table 2:]

Concentration and Size Distribution of Microbubbles.

	MicroMarker	BR38	Definity	Sonovue
Concentration, 10^8/mL	2.0±0.3	23.9±10.7	9.4±1.9	2.6±2.5
95% size range, μm	1.5–2.9	1.3–2.7	1.5–3.6	1.2–2.2
Mean diameter, μm	2.0±0.4	1.9±0.4	2.0±0.1	1.8±0.5
Median diameter, μm	1.9±0.1	1.7±0.1	2.2±0.6	1.7±0.1

[Table 3:]

Selected Ultrasound Parameters Used for Therapy.

US Parameter	***In vivo*-optimized**	**Phantom-optimized**
PRF, Hz	1	100
Voltage, V	70	90
PNP, MPa	3.4	4.4
MI	1.22	1.54
Therapy time, sec	100	100
No of Therapy Pulses	100	10,000